Journal of Industrial and Engineering Chemistry 131 (2024) 199–207

Contents lists available at ScienceDirect

Journal of Industrial and Engineering Chemistry

journal homepage: www.elsevier.com/locate/jiec

Enhanced Nitrogen-Doped Reduced Graphene Oxide-Embedded $MnMoO_4$ as High-Capacity and Stable Anode for Sodium-Ion Batteries

Seo-Jun Lee [a], Megala Moorthy [a], Sangho Park [b,*], Yun-Sung Lee [a,*]

[a] School of Chemical Engineering, Chonnam National University, Gwangju 61186, Republic of Korea
[b] Department of Battery Engineering, Dongshin University, Naju-si, Jeollanam-do 58245, Republic of Korea

ARTICLE INFO

Article history:
Received 6 September 2023
Revised 26 September 2023
Accepted 6 October 2023
Available online 13 October 2023

Keywords:
Sodium ion batteries
$MnMoO_4$ nanorods
N-doped reduced graphene oxide
Ternary metal oxides

ABSTRACT

Nanostructures of ternary metal oxides have been modified with nitrogen-doped reduced graphene oxide (rGO) to enhance electronic conductivity and also effectively mitigate volume variations in anodes used for sodium-ion batteries (SIBs). Unlike bimetallic metal oxides, ternary metal oxides undergo multiple redox reactions, resulting in high capacity. However, the effective anode type, $MnMoO_4$ (MTMOs), is significantly challenged by volume expansion and contraction issues throughout the charge and discharge process, which leads to capacity decay and poor cyclability in SIBs. In this study, we report an N-doped rGO-embedded $MnMoO_4$ composite as an excellent anode, that can withstand the volume accommodation related issue due to numerous active sites in $MnMoO_4$. The as-prepared $MnMoO_4$@rGO@g-C_3N_4 composite electrode exhibited a capacity of 135 mAh g^{-1} after 800 cycles at a high current density of 1 A g^{-1} and, the cell retained 58.2% of its initial capacity even after 900 cycles. The N-doped rGO-embedded $MnMoO_4$ demonstrates superior electrochemical properties and holds promise as the next-generation anode material for sodium-ion batteries.

Introduction

Lithium-ion batteries (LIBs) have emerged as satisfactory energy storage devices for high-power electric and electronic applications, especially in portable devices. However, due to the limited availability of lithium resources and its toxicity, the sustainability of large-scale LIB production remains a topic of debate [1,2]. Consequently, with these significant challenges, the demand for energy storage devices has surged in recent years, driven by their potential in zero-emission transportation applications. Accordingly, alternative systems are under an extensive investigation to replace rechargeable batteries, because current systems may not meet the growing demands of the future. Therefore, sodium-ion batteries (SIBs) are regarded as the promising options to replace LIBs, due to the high abundance of sodium and their affordability [3–6]. In addition, the chemical and electrochemical reactions of sodium closely resemble those of lithium in most electrode materials [7,8]. However, the atomic radius of sodium ion is bigger than lithium, which leads to significant volume expansion and contraction issues[9] Consequently, current research is focused on finding suitable anode materials for SIBs and recently developed mixed transition ternary metal oxides (MTMOs) have shown promising outcomes in various applications due to their flexible structures and high theoretical capacity of (between 600 –1000 mAh g^{-1}) [12,13]. Notably, MTMOs, such as $CoMoO_4$ [11], $FeMoO_4$ [12], $NiMoO_4$ [13], $MnMoO_4$ [14], and $ZnMnO_4$ [15], composed of two metallic elements, offers synergistic effect with multiple redox reactions, achieving a practical capacities exceeding 500 mAh g^{-1}. Among these anode materials for sodium-ion batteries, $MnMoO_4$ stands out as an appealing candidate for practical applications due to its non-toxicity and excellent electrochemical performance [10]. Based on the synergistic effect of the two metal oxides in $MnMoO_4$, it can exist in different oxidation states (2^+ & 6^+), exhibiting a high sodium reversibility with higher capacity at lower potential. However, $MnMoO_4$-based anode exhibits poor cyclability and rapid capacity decay due to their low electronic conductivity [16]. To address these restricted limitations, carbon with $MnMoO_4$ structure is constructed as a SIB anode, because carbon-based materials renders a large surface area and high conductivity when doped into the $MnMoO_4$ structure [17]. Generally, carbonaceous materials such as carbon nanotubes, graphene, and carbon fibers are widely used to coat on TMOs. These materials do not undergo redox reactions but serves as a coating layer with

* Corresponding authors.
E-mail address: leeys@chonnam.ac.kr (Y.-S. Lee).

https://doi.org/10.1016/j.jiec.2023.10.019
1226-086X/

a large surface area, preventing side reactions with the electrolyte. Their high porosity creates abundant pathways for storing sodium ions. So, it can efficiently reducing the stress level during charge/discharge cycles, maintaining stable structures, and facilitating smooth sodium ion transportation. Additionally, it can able to tolerate the volume fluctuations during cycling and enhances the electronic conductivity slightly more than the pristine $MnMoO_4$ structure [21]. For instance, Wu et al. [18] demonstrated the use of reduced graphene oxide (rGO) with $NiFe_2O_4$ to construct a composite anode for SIBs. Notably, carbon coating can modify the outer layer structures without significantly affecting the bulk properties of metal oxides. Consequently, the $NiFe_2O_4$/rGO-based anode exhibited a discharge capacity of 450 mAh g^{-1}, which was double that of pristine $MnMoO_4$; however, the cycle stability was limited to 50 cycles. Yang et al. [19] combined $CoMoO_4$ with graphene sheets, achieved a discharge capacity of 646 mAh g^{-1} at a current density of 5 A g^{-1}, with stable cyclability up to 200 cycles [20,21]. However, it's important to note that effective carbon coating on transition metal oxides (TMOs) may not always significantly improve electrical conductivity. Furthermore, battery cycle life is considered a crucial factor in practical applications. So,to enhance cycle stability, nitrogen doping in carbonaceous materials has proven to be an effective strategy. This approach increases electronic conductivity to a significant extent and mitigates volume expansion and contraction of electrodes, to extend their cycle life [22]. In that concern, current research is primarily focused on developing heteroatom materials to further enhance electronic conductivity and employed carbon coating to increase surface area, thereby expanding the active sites for sodium ion storage. Non-metallic graphitic carbon nitride (g-C_3N_4), derived from melamine as the parent material, which is commonly used as a precursor for nitrogen doping due to its rich nitrogen content compared to other sources. This unique property, along with a significant number of defects, can further increase the active sites for sodium [23,24,6]. Specifically, nitrogen-based functional groups influence the redox reactions that occur in the electrode and by altering the electronic structure of $MnMoO_4$, leading to additional pseudo capacitance for fast sodium ion transport with overall improved capacity performance. Nitrogen doping not only increases the reversible capacity of the anode, but also preserves its structural integrity over a time. With improved charge storage properties, this well-maintained anode can lead to long-term cycle stability in sodium-ion batteries. Additionally, nitrogen-doped $MnMoO_4$ reduces reliance on toxic materials, making it an environmentally sustainable choice for battery production [25–28]. Huang et al. [29] incorporated N-doped carbon into an $CoMoO_4$ effective anode for sodium-ion batteries. A half-cell exhibited a reversible capacity of 190 mAh g^{-1}, with outstanding cycle stability over 3200 cycles. Further, Shanthappa et al. [30] proposed N-doped rGO with cobalt molybdate as potential anode candidates for LIBs. These electrodes presented a discharge capacity of 612 mAh g^{-1}, also demonstrating an efficient performance of up to 250 cycles. The previously reported results indicate that N-doping defects on the active material result in an effective structural electrode. The electrode surface area is larger when both carbon coating and nitrogen doping are combined, rather than those obtained by only carbon coating (or only nitrogen doping) [31]. The aforementioned findings have motivated us to explore N-doped rGO with $MnMoO_4$ as potential anode candidates, aiming to achieve superior performance and prolonged cycle life in SIBs [32,33].

In this study, we have focused on designing a composite anode consisting of graphitic carbon nitride (g-C_3N_4) doped into reduced graphene oxide (rGO), later which was then embedded into the mixed metal oxide $MnMoO_4$. The nanorod morphology-based nitrogen-enriched anode with carbon coating efficiently reduces charge transfer resistance during the transport of sodium ions. The uniform coating of carbon and nitrogen doping significantly enhances both structural stability and electronic conductivity. We conducted various chemical and electrochemical studies to investigate the electrochemical studies of the optimized anodes. The as-received $MnMoO_4$@rGO@g-C_3N_4 electrode exhibited improved capacity and long-term cyclability, thus making it a favorable anode candidate for sodium-ion batteries.

Experimental details

Materials

Manganese acetate tetrahydrate ($C_4H_6MnO_4.4H_2O$-Aldrich) Ammonium molybdate tetrahydrate $(NH_4)_6Mo_7O_{24}$-$4H_2O$ Sigma Aldrich), melamine ($C_3H_6N_6$, Sigma Aldrich), and Graphene oxide (GO-V20 STARD, Inc) used as received and all the chemicals were purchased form South Korea.

Methods

Synthesis of $MnMoO_4$

Pristine $MnMoO_4$ was synthesized by a liquid-phase method. First, ammonium molybdate tetrahydrate $(NH_4)6Mo_7O_{24}.4H_2O$) and manganese acetate tetrahydrate ($C_4H_6MnO_4.4H_2O$) were stirred and separately dispersed in 25 mL of distilled water. Next, the ammonium molybdate solution was slowly poured into the manganese acetate solution and stirred for 4 hours at 50 °C. The obtained powder washed various times with distilled water and ethanol to remove traces from on it. Subsequently, the synthesized yellow powder of $MnMoO_4H_2O$ was vacuum-dried at 80 °C for more than 12 h and then kept on alumina boat and heated at 500 °C (heating rate: 2 °C/min) for 2 h under a N_2 gas atmosphere using a tube-type firing furnace. The final product was pulverized for 10 min using a mortar to obtain the rod-type $MnMoO_4$ anode active material.

Synthesis of graphitic carbon nitride(g-C_3N_4)

Initially, 1 gram of melamine ($C_3H_6N_6$) powder was placed on alumina boat and heated treated at 550 °C, 2°C/min using a tubular firing furnace under an argon atmosphere. After heating, a yellow powder was obtained and ground for 10 minutes using a mortar and pestle. Later graphitic carbon nitride (gC_3N_4) was synthesized and added as an additive.

Synthesis of N doped rGO embedded $MnMoO_4$

Firstly, 4 mg g-C_3N_4, 10 mg GO, and 200 mg of $MnMoO_4$ was prepared and then added to 50 ml of DI water; the resulting solution was stirred 2 h continuously and subsequently transferred to a sonicator to ensure thorough dispersion of all three substance. Next, the mixed solution was poured into a 200 mL Teflon-lined autoclave and sintered at 120 °C for 24 h. In further, the obtained solution was washed with DI water and ethanol and residues were vacuum-dried at 80 °C for approximately 12 h. Finally, the received powder was calcinated for 2 hour at 400 °C under a nitrogen gas atmosphere to obtain a product of $MnMoO_4$@rGO@g-CN composite anode.

Physical and chemical characterization equipments

A High-resolution X-ray diffraction (HR-XRD, D/MAX Ultima III, Rigaku Co., Japan) study was performed to examine the crystal structure of the synthesized anode. The morphologies of pristine $MnMoO_4$ and nitrogen/carbon coated $MnMoO_4$ were inspected by (FESEM, S-4700, Hitachi Co., Japan), field-emission scanning electron microscopy. The presence of rGO in the composite electrodes

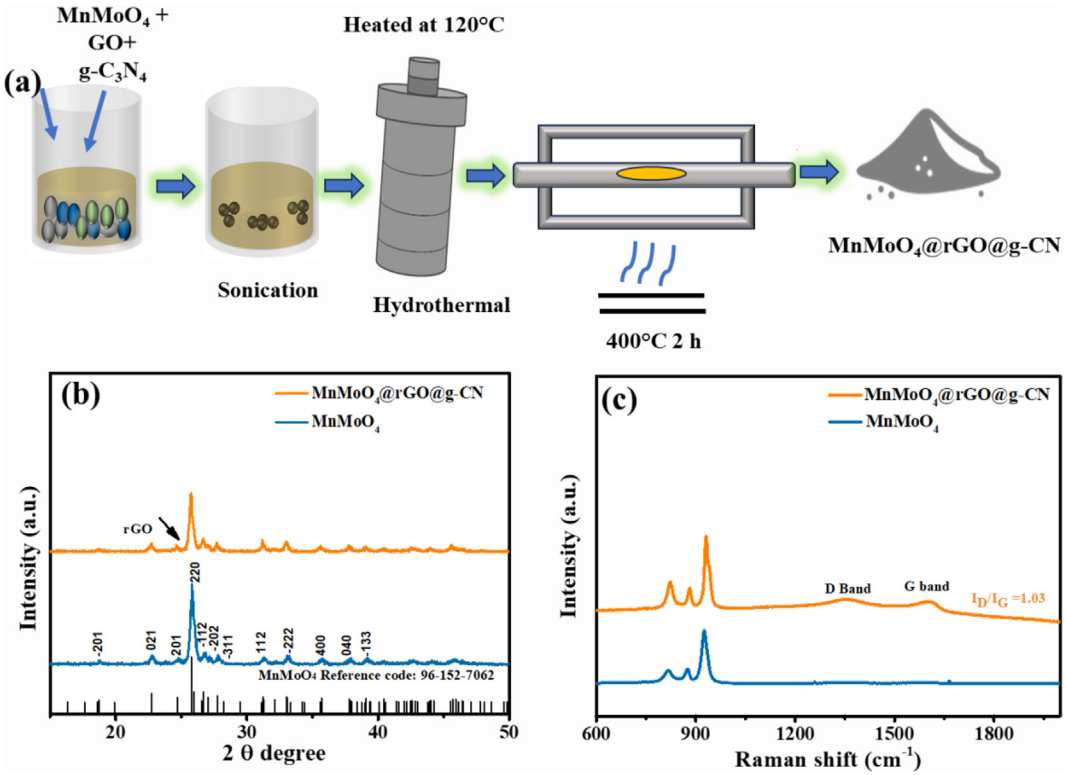

Fig. 1. (a) Schematic of the synthesis of $MnMoO_4$@rGO@g-CN composite material by a liquid-state reaction. (b) XRD patterns of $MnMoO_4$ and $MnMoO_4$@rGO@g-CN.(c) Raman spectra of $MnMoO_4$, and $MnMoO_4$/rGO@g-CN.

was analyzed specially using a Raman spectrophotometer (NRS-5100, JASCO, Inc, Japan). Thermogravimetric analysis (TGA, TGA-50, Shimadzu, Japan) was performed to verify the carbon content in the composite material. X-ray photoelectron spectroscopy (XPS, MultiLab2000, VG, UK) was implemented to analyze the composition of elements along with nitrogen/carbon bonding states.

Electrochemical measurement

The chemical and electrochemical experiments of the synthesized both pristine $MnMoO_4$ and $MnMoO_4$@rGO@g-C_3N_4 materials were conducted using a CR2032 coin cell. To prepare the working electrode, 5 mg of the active material ($MnMoO_4$), 1 mg of a conductive material (ketjen Black Co, Japan), and 1 mg of Teflonized acetylene black were mixed in a mortal piztal. The mixture was then placed over a stainless steel mesh based current collector and dried at 160 °C, 4 h at a vacuum filled oven,respectively For coin cell fabriation, pure Na metal as counter electrode, polypropylene film as a porous separator, and 1 M $NaPF_6$ diglyme (KISHIDA CHEMICAL, Japan) was used as electrolyte .. All the electrodes were tested using the coin cell and performed inside a glove box under an argon atmosphere. The coin cell was subjected to charge and discharge cycles in the 0.01–3 V *vs*. Na window. The cycling characteristics were rated at different current density of 1000 and 200 mA g^{-1}. Further, the electrodes subjected to perform the cyclic voltammetry (CV) at a scan rate of 0.1 mV s^{-1} within the same potential window of 0.01–3 V *vs*. Na.

Results and discussion

Fig. S1 schematically illustrates the synthesis procedure of pristine $MnMoO_4$ (a mixed metal oxide) by a liquid-phase method. To prepare the nitrogen doped carbon embedded $MnMoO_4$ anode, manganese acetate tetrahydrate and ammonium molybdate tetrahydrate were used as the precursor sources for manganese and molybdate. Then, melamine is used as the precursor to receive a graphitic carbon nitride as a nitrogen source, because it has a high nitrogen source (N_6) respectively. Initially, different weight percentages of GO (0, 5, and 8 wt.%) and g-C_3N_4 (0,2, 3, 4, and 5 wt%) were optimized to determine their effective ratios with pristine $MnMoO_4$ [34], and then 5 wt.% of GO and 2 wt.% of g-C_3N_4 were recognized as the optimal concentrations. At first, manganese acetate and ammonium molybdate were well interlinked with graphene oxide via stirring process. Later, GO was converted into rGO via conversion reactions at 120 °C for 24 h during the calcination process. The sheet like a reduced graphene oxide has large surface area, which could be the important factor to consider it. Later, then, 2 wt.% of the optimized amount of melamine was poured into the above mixture. The composite mixture was then calcinated at (400 °C, 2 h) under an argon-gas atmosphere, to receive a $MnMoO_4$@rGO@g-CN, schematic as presented in Fig. 1 (a), Reduced graphene oxide coated and nitrogen doped $MnMoO_4$, could provide the more active sites due to their high surface area and nitrogen is attached to the edges of rGO sheets during the calcination process. Finally, N-doped rGO matrix successfully merged with the $MnMoO_4$.The samples obtained at each process steps, namely pristine $MnMoO_4$, and the final product of $MnMoO_4$@-rGO@g-CN, were separately collected for comparison reason. The crystal structure and phases of two prepared sample were analyzed by XRD study, and corresponding profile is presented in Fig. 1(b). The diffraction peaks are indexed and well-matched with those of the pristine $MnMoO_4$ reference structure in the monoclinic-type C12/m1 phase. Further, no impurity peak is observed in the profile of the synthesized compound and the calculated lattice constant values are a = 10.4690, b = 9.5160, and c = 7. 1430 Å, which are consistent with those reported previous work [35]. Prominent peaks are detected at 22.8°, 24.7°, 25.8°, 26.9°,

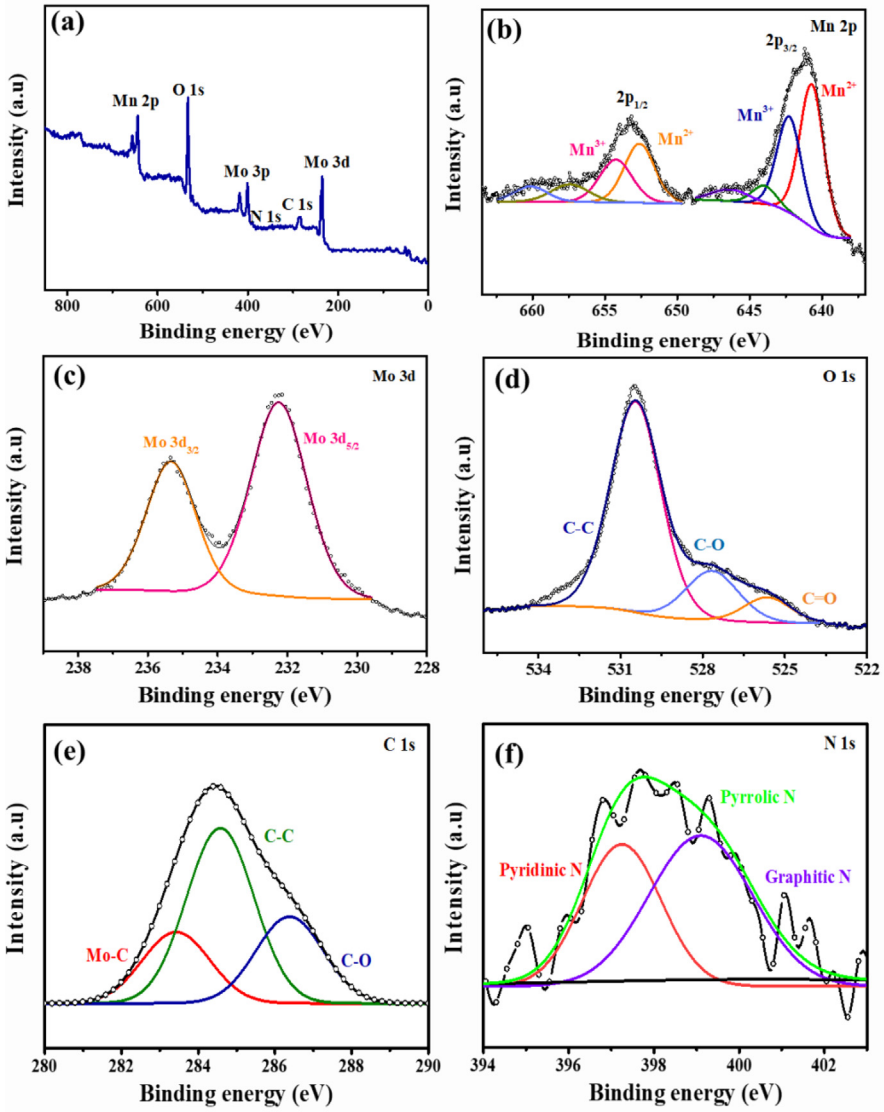

Fig. 2. (a) Survey XPS spectra of $MnMoO_4$@rGO@g-CN; XPS spectra of (b) Mn 2p, (c) Mo 3d, (d) O 1s, (e) C 1s, and (f) N 1s.

27.8°, 31.3°, and 33.1°, which correspond to the planes of (0 2 1), (2 0 1), (2 2 0), (−1 1 2), (−3 1 1), (1 1 2), and (−2 2 2), respectively [36]. The XRD results confirm that, as prepared composite anode is have all three phases with high crystallinity and structurally stable. In further Fig. 1(c) presented the Raman spectra of all samples, the characteristic peak of the pristine $MnMoO_4$ nanostructure are located at 932, 876, and 820 cm^{-1} [37] and some additional peaks are visible at 1359,1590 cm^{-1}, which can be ascribed to the defective (D) and graphitic bands (G) of the reduced graphene oxide [38,39]. The observed peak shifting can be attributed to the formation of rGO composite, which exhibits disordered characteristics of amorphous carbon [40]. So, Intensity ratio of the D and G bands (I_D/I_G) displays the presence of defects in the nanostructure [41]. For the $MnMoO_4$@rGO@g-CN electrode I_D/I_G ratio is (1.03), which marginally increases for N-doped rGO rather than pristine $MnMoO_4$ [42–44]. It's clearly indicates that N-doping is crucial for introducing more defects and increasing the electronic conductivity through covalent bonding between the carbon and edged nitrogen atoms [45,46]. Raman spectra study shows that large no of defects, so that it could store the more Na ions in its structure. To investigate the decomposition of carbon content in the $MnMoO_4$@rGO@g-CN composite, Thermo gravimetric analysis (TGA) was performed, corresponding results are presented in Fig. S2. The results clearly show that, the decomposition peak observed at 350 °C in which weight loss of carbon content is 7 wt.% [10].

To investigate the chemical states and composition of the as-prepared $MnMoO_4$@rGO@g-CN composite anode, analyzed the XPS study. Fig. 2 shows the elemental distribution of the electrode. Fig. 2(a) presents the elements survey spectra, including Mn 2p, Mo 3d, O 1s, C 1s, and N 1s. The high resolution Mn 2p peaks located at 640.75 and 652.6 eV which are ascribed to Mn $2p_{3/2}$ of Mn^{2+} and Mn $2p_{1/2}$ of Mn^{3+}, respectively, as presented in Fig. 2 (b) [47]. The high-resolution Mo 3d spectrum shows two peaks found at 232 and 235 eV, which arise from Mo $3d_{5/2}$ and Mo $3d_{3/2}$, respectively [48,49] as presented in Fig. 2(c). O 1s spectrum is deconvoluted into two peaks at 530 and 528 eV, which can be attributed to Mo—O and C═O bands, respectively [50] (Fig. 2(d)). The C 1s spectrum is deconvoluted into three peaks at 283.5, 284, and 286.2 eV, corresponding to the Mo—C, C—C, and C—O bands, as presented in Fig. 2(e) [51]. The Mn—C peak at 283.1 eV indicates that strong interactions between rGO and $MnMoO_4$ [52]. Fig. 2(f) shows that the N 1s spectra are deconvoluted into three peaks at 398.3, 400.2 and 401.5 eV, corresponding to pyridinic, pyrrolic, and graphitic nitrogen, respectively [21,53]. The

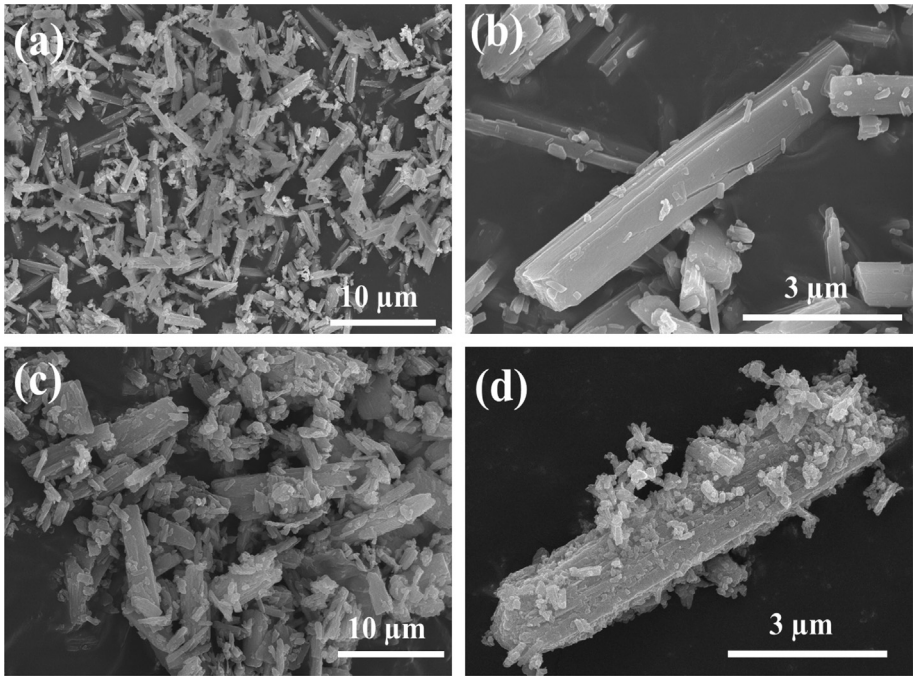

Fig. 3. Surface morphology of composite electrode of (a&b) pristine $MnMoO_4$ and (c&d) $MnMoO_4$@rGO@g-CN.

above mentioned XPS results confirm the effective doping of nitrogen (source: g-C_3N_4) into rGO embedded $MnMoO_4$ matrix. Numerous investigations of nitrogen species have been conducted, because nitrogen doping offers a significantly high electronic conductivity. Further, nitrogen can easily attach to the edges of carbon, thereby effectively creating many defects in the structure. Therefore, mixing of carbon and nitrogen in pristine $MnMoO_4$ nanostructures results in a synergistic effect, which is expected to expand the Na-ion storage capacity in $MnMoO_4$-based electrode [54].

The as prepared N doped carbon embedded nanorods are obtained by simple liquid phase reaction method. After the calcination process, internal morphology with coating and doping of the $MnMoO_4$@rGO@g-CN and pristine $MnMoO_4$ were analyzed by FESEM study, and the corresponding images are presented in Fig. 3(a) Pristine $MnMoO_4$ shows a rod-like surface morphology, whereas the particle is agglomerated evenly and Fig. 3(b) From the zoomed view of SEM images shows that single nanorods are very smooth and clear, where there is no additional reaction. In meanwhile, the nitrogen doped rGO embedded $MnMoO_4$ matrix exhibits a rough surface Fig. 3(c) and (d), which can be mainly ascribed to the influence of the g-CN bonded carbon particles uniformly embedded on the rod-like $MnMoO_4$. The high interconnectivity between nitrogen and carbon atoms creates the more surface-to-surface conducting pathways, thereby improving the conductivity [55]. To evaluate the internal morphology and microstructure of the $MnMoO_4$@rGO@g-CN composite anode, Fig. 4 presents results of TEM, high-resolution TEM (HR-TEM), and (EDS) analysis presented in Fig. 4(a) TEM images show that, $MnMoO_4$ nanorods are well interlinked with reduced graphene oxide nanoparticle. The HR-TEM images presented in Fig. 4(b) indicate the existence of a 5–10-nm-thick carbon layer over the surface of $MnMoO_4$. In addition, the interlayer spacing (d) is 0.502-nm corresponding to the (2 0 0) crystal plane of monoclinic $MnMoO_4$ and provides more insights into the crystal structure. The EDS mapping results presented in Fig. 4(c) demonstrate that the elements Mn, Mo, O, C, and N are uniformly distributed over the $MnMoO_4$@rGO@g-CN composite [41]. From EDS results, homogeneously coated nitrogen and carbon provides the highly stable internal structure to the $MnMoO_4$ matrix. Consequently, due to high electronic conductivity, no of active sites are increasing to store the more sodium ions effectively [56].

The electrochemical studies were conducted to assess the electrochemical performance of the as-prepared $MnMoO_4$@rGO@g-CN anode,along with the pristine samples for comparison and the results are presented in Fig. 5. The CV analysis of the $MnMoO_4$@rGO@g-CN composite electrode was performed at 0.1 mV s^{-1} scan rate between 0.1 to 3.0 V *vs*. Na Fig. 5(a). During initial cycles, irreversible peaks are detected at 0.38, 0.87, and 0.97 V *vs*. Na, indicating inevitable side reactions resulting in a solid electrolyte interphase layer and poor coulombic efficiency [57]. However, when the cycle number increases, all the curves overlay with each other, representing the excellent reversibility with a prolonged cycle life for SIBs. The absence of sharp peaks in the subsequent CV curve can be attributed to an irreplaceable reaction that predominantly occurs in first cycle [20]. All the observed peaks correspond to anodic and cathodic reaction. The possible reaction mechanism is as follows:

$$MnMoO_4 + 8Na \rightarrow Mn^0 + Mo^0 + 4Na_2O \quad (1)$$

$$Mn^0 + Na_2O \rightarrow MnO + 2Na \quad (2)$$

$$Mo^0 + 3Na_2O \rightarrow MoO_3 + 6Na \quad (3)$$

Galvanostatic charge–discharge analyses of the pristine $MnMoO_4$ and $MnMoO_4$@rGO@g-CN samples were performed at 200 mA g^{-1} to further examine the Na ion storage properties. The discharge capacities of pristine $MnMoO_4$ are 376, 240, 188, 187,184 and 174 mAh g^{-1} at the first, second, 50th, 100th, 150th and 200th cycles, presented in Fig. S3. The low coulombic efficiency observed in the first cycle can be principally assigned to forming an uneven SEI layer over the electrode surface [2]. As expected, pristine $MnMoO_4$ resulting capacities are low owing to the two metals Mn and Mo, with low electronic conductivities, and a simple structure could not sustain the large volume expansion and contraction issues throughout the cycling process [15]. In contrast, the $MnMoO_4$@rGO@g-CN cell gives relatively high

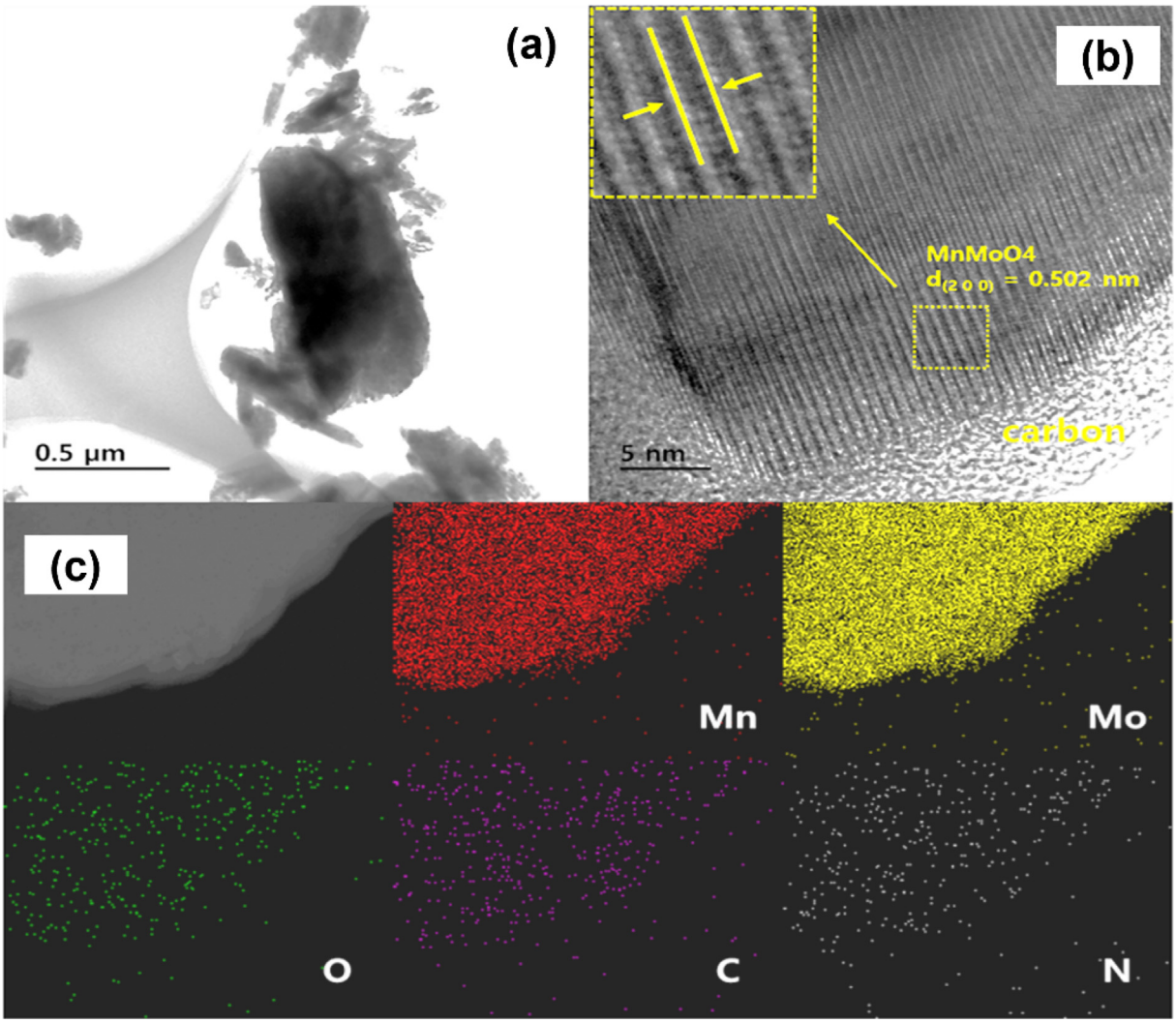

Fig. 4. (a)TEM image of $MnMoO_4$@rGO@g-CN, (b) HR-TEM image, and (c) EDS mapping image of individual elements (Mn, Mo, O, C, and N).

charge and discharge capacity of 286 and 470 mAh g^{-1}, as presented in Fig. 5(b). The observed higher discharge capacity of the $MnMoO_4$@rGO@g-CN electrode during the primary cycles can be potentially recognized to the large number of conductive routes provided by the active sites of rGO@g-CN bonding, with large surface area. Contrarily, the composite electrode $MnMoO_4$@rGO@g-CN exhibits excellent discharge capacities of 470, 286, 224, 222,219and 230 mAh g^{-1} at first, second, 50th, 100th, 150th, and 200th cycles, respectively. The observed higher capacity of the $MnMoO_4$@rGO@g-CN composite electrodes is primarily ascribed to the carbon/nitrogen bonding. The nitrogen doping induces electronic conductivity and improves the diffusion kinetics faster near the electrode surface to maintain rapid Na ion transportation [55].

In further, Fig. 5(c) displays the rate capability of both the pristine $MnMoO_4$ and composite electrodes at different current densities (varied from 0.1 to 2 & 1 A g^{-1}). The $MnMoO_4$@rGO@g-CN composite electrode demonstrates excellent capacities of 288, 251, 219, 193,164 and 241 mAh g^{-1} at 0.1, 0.2, 0.5, 1 and 2 A g^{-1}, respectively. These capacity values are significantly higher than those of the pristine $MnMoO_4$ electrode (237, 200, 176, 151, and 144 mAh g^{-1} and 198 mAh/g respectively; analysis performed using the same procedure). From the above results, our $MnMoO_4$@-rGO@g-CN electrode can give an excellent rate capability attributed to its structural stability and good Na ion storage reversible capacity [58]. Subsequently, both electrodescycling stability were validated at a 200 mA g^{-1} current density. The discharge capacity of pristine $MnMoO_4$ is 235 mAh g^{-1} during the initial cycle, and after 250 cycles, it significantly reduces to 154 mAh g^{-1}. These values are lower than those of the $MnMoO_4$@rGO@g-CN electrode, which displays discharge capacity of 471 mAh g^{-1}in first cycle and 290 mAh/g during second cycle. After 200 cycles, the $MnMoO_4$@rGO@g-CN electrode retains 80.7% of its initial capacity, which is more than that retained by the pristine $MnMoO_4$ electrode (51.6%). During the initial cycles, capacity decay obtained due to the formation of un even SEI layer, up to 100 cycles [59], as presented in Fig. 5(d). Our nitrogen doped carbon embedded $MnMoO_4$ electrode improves the cycle stability at 200 mA g^{-1}current density. Notably, even after 100 cycles, the composite $MnMoO^4$@rGO@g-CN electrode achieved a 99.8% columbic efficiency with a discharge capacity of 224 mAh/g, whereas the discharge capacity of pristine $MnMoO_4$ was 191 mAh/g with 98.5% efficiency in Fig. S4.

Further, to elucidate the effect rGO and g-CN addition in the $MnMoO_4$ matrix, a rate study was separately performed in a different ratios, and the corresponding results are presented in Figs. S5 and S6**.** By varying the percentage of graphene oxide with $MnMoO_4$, thickness is slightly varied, in accordance with cyclability. However, moderate thickness with (5 wt %) provides a stable

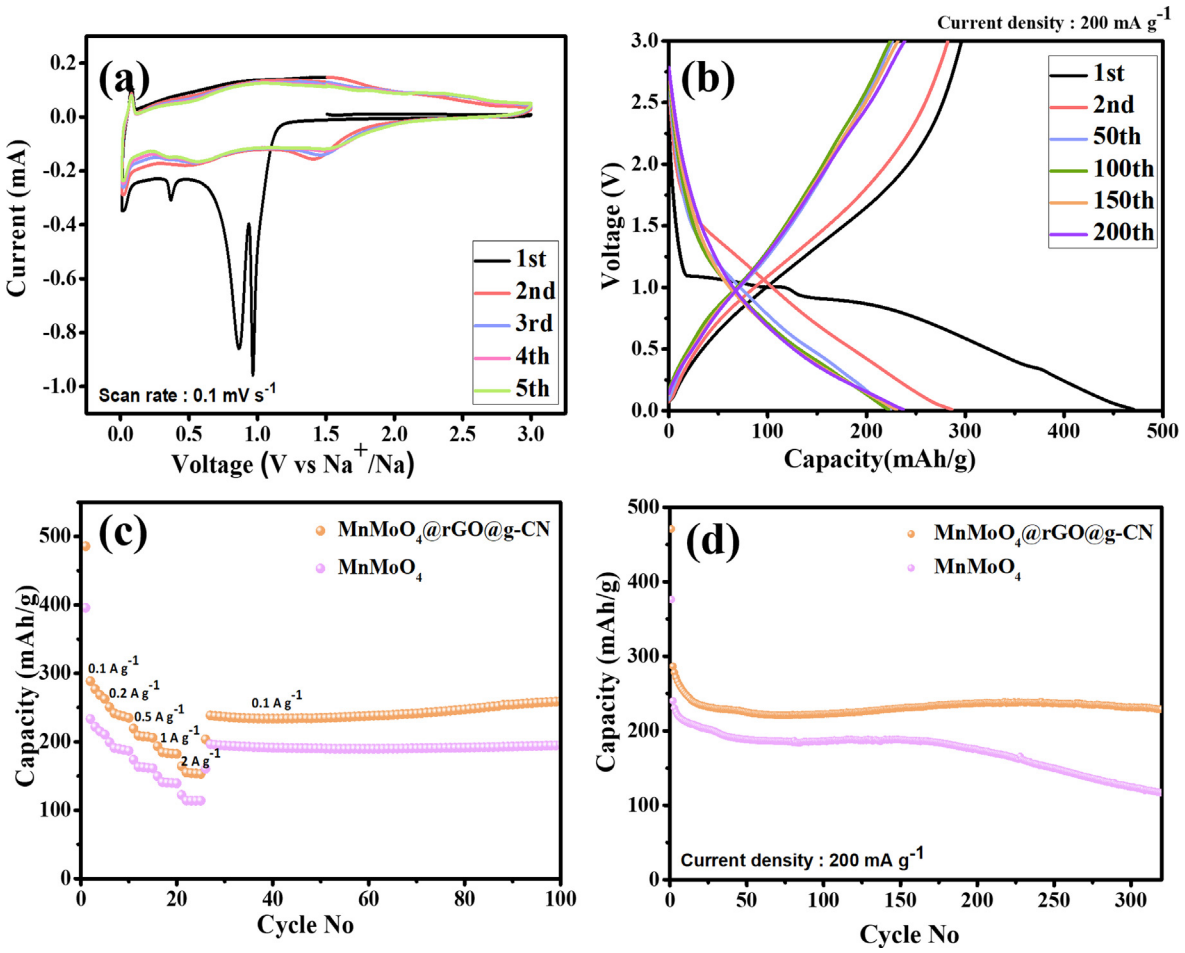

Fig. 5. (a) CV profiles of $MnMoO_4$@rGO@g-CN at a scan rate of 0.1 mV s^{-1}. Charge–discharge curves of (b) $MnMoO_4$@rGO@g-CN at a current density of 200 mA g^{-1}. (c) Cyclability of $MnMoO_4$ and $MnMoO_4$@rGO@g-CN at a current density of 200 mA g^{-1}. (d) Rate capability of pristine $MnMoO_4$ and $MnMoO_4$@rGO@g-CN at 200 mA g^{-1}.

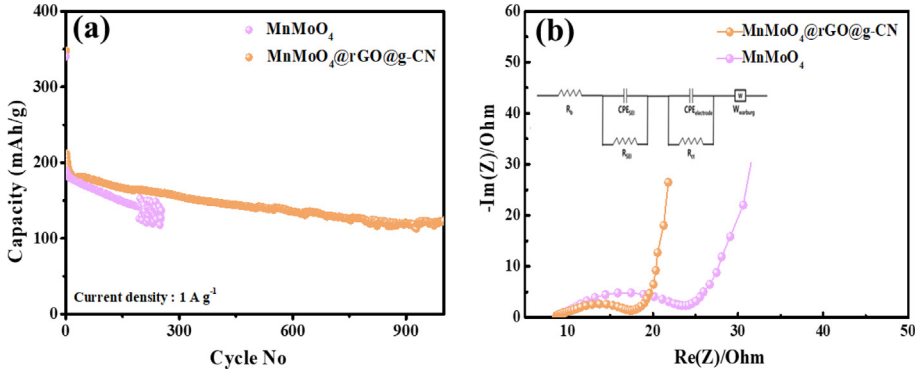

Fig. 6. (a) Cyclability of $MnMoO_4$ $MnMoO_4$@rGO@g-CN at a current density of 1 A g^{-1} and (b) Nyquist plots of both $MnMoO_4$ and $MnMoO_4$@rGO@g-CN.

electrochemical performance as increasing with several no of cycles. Since the optimal thickness of carbon coating could employed the stable and thin layer to increase the capacity [60]. Fig. S5 [58]. In the next step, graphitic carbon nitride varied in different weight % and checked their compatibility with both 5 wt % GO and $MnMoO_4$ as presented in Fig. S6. The optimized 2 wt % g-CN, provides a decent charge/discharge capacities as increasing with many cycles. The initial slow capacity obtained might be mainly associated with the structural activation process and it started increasing with the cycle no increases in later. The minimal thickness of graphitic carbon coating could only induce the many defects in the structure, rather than increase the charge transfer resistance. The observed outstanding electrochemical performance of the $MnMoO_4$@rGO@g-CN electrode can be accredited to two factors: (1) Improved electrical conductivity of covalently bonded rGO@g-CN structure, and (**2**) Uniform ion distribution due to abundant pores and it can be able to suppress volume expansion. Moreover, the above mentioned electrochemical results demonstrate the high stability and reversible capacity of $MnMoO_4$@rGO@g-CN [61,62].

In most cases even though the capacity is higher in terms, still cycle stability also important factor to be considered for the prac-

tical applications of batteries [21]. Fig. 6 displays the long-term cycle stability of $MnMoO_4$@rGO@g-CN and pristine $MnMoO_4$ at high current density of 1 A g^{-1}; the electrodes exhibits discharge capacities of 218 & 188 mAh g^{-1}, respectively. However, after 200 cycles, the stability of the pristine $MnMoO_4$ electrode decreases significantly, and its discharge capacities decreases to < 100 mAh g^{-1}. Also, poor columbic efficiency may be due to the unstable SEI film with structural collapses near to the anode side. By contrast, the $MnMoO_4$@rGO@g-CN composite electrode exhibits excellent stability in decreasing order and increased after several cycles. It may be due to the intial activation process, during charge and discharge process and its stable up to 1000 cycles Fig. 6 **(a)**. Further, our composite anode retained up to 58.2% of its retention capacity even after 900 cycles. Furthermore, electrochemical impedance spectroscopy was performed to investigate both electrodes reaction kinetics. Fig. 6**(b)** presents the Nyquist plots of $MnMoO_4$ and $MnMoO_4$@rGO@g-CN, indicating the electrode charge transfer resistance and diffusion mechanism. The semicircle observed in the high-frequency region signifies the interfacial resistance, whereas the straight line observed in the low-frequency region symbolizes the ion diffusion resistances of the $MnMoO_4$ and $MnMoO_4$@rGO@g-CN electrodes. The fitted interfacial resistance of $MnMoO_4$@rGO@g-CN is 17.44 Ω, which is notably lower than that of $MnMoO_4$ (23.46 Ω) and is associated with the covalent bonding between rGO and g-CN. This bonding enhances the electronic conductivity and promotes the formation of a robust interface in the middle of the electrode and electrolyte interphase [16]. The Nyquist plots reveal that charge transfer resistance of the fabricated $MnMoO_4$@rGO@g-CN composite anode is lower than pristine $MnMoO_4$ electrode; further, the diffusion kinetics of the composite anode are better than those of the pristine $MnMoO_4$ electrode. The above results indicate that the composite electrode is completely carbon coated with a nitrogen edge, which diminishes the induced stress in structure [30,5].

Conclusion

In summary, we have successfully synthesized g-CN-doped rGO embedded $MnMoO_4$ nanorods by a hydrothermal method. N-doped carbon increased the number of structural defects, resulting in improved Na ion storage. The different weight percentages of g-CN and rGO with $MnMoO_4$ were optimized and capacity of the $MnMoO_4$@rGO@g-CN electrode was found to be higher than those of pristine $MnMoO_4$. Specifically, after 200 cycles the discharge capacity of pristine $MnMoO_4$ and $MnMoO_4$@rGO@g-CN were 124 and 231 mAh g^{-1}, at 200 mA g^{-1}. While current density raised to 1 A g^{-1}, pristine $MnMoO_4$ and as-prepared electrode of $MnMoO_4$@-rGO@g-CN demonstrated an initial discharge capacity of 188 and 218 mAh g^{-1}. Further the fabricated electrode maintained 58.2% of its initial capacity even after 800 cycles. The improved electrochemical performance of the as-prepared electrode can be ascribed to the synergistic effect of carbon and nitrogen doping, which introduces more defects and thus enhances the sodium-ion storage capacity.

Declaration of Competing Interest

The authors declare that they have no known competing financial interests or personal relationships that could have appeared to influence the work reported in this paper.

Acknowledgement

This work was supported by the National Research Foundation of Korea (NRF) grant funded by the Korean government (Ministry of Science, ICT & Future Planning) (No. RS-2023-00208361).

Appendix A. Supplementary material

Supplementary material to this article can be found online at https://doi.org/10.1016/j.jiec.2023.10.019.

References

[1] Q. Pan, D. Gong, Y. Tang, Energy Storage Mater. 31 (May) (2020) 328–343, https://doi.org/10.1016/j.ensm.2020.06.025.
[2] R. Thangavel, A. Samuthira Pandian, H.V. Ramasamy, Y.S. Lee, ACS Appl. Mater. Interfaces 9 (46) (2017) 40187–40196, https://doi.org/10.1021/acsami.7b11040.
[3] M.H. Cao, Z. Shadike, S.M. Bak, T. Wang, E. Hu, S. Ehrlich, Y.N. Zhou, X.Q. Yang, Z.W. Fu, Energy Storage Mater. 24 (July 2019) (2020) 417–425, https://doi.org/10.1016/j.ensm.2019.07.022.
[4] S.P. Ong, V.L. Chevrier, G. Hautier, A. Jain, C. Moore, S. Kim, X. Ma, G. Ceder, Energ. Environ. Sci. 4 (9) (2011) 3680–3688, https://doi.org/10.1039/c1ee01782a.
[5] A. Abouimrane, W. Weng, H. Eltayeb, Y. Cui, J. Niklas, O. Poluektov, K. Amine, Energ. Environ. Sci. 5 (11) (2012) 9632–9638, https://doi.org/10.1039/c2ee22864e.
[6] R. Thangavel, B.K. Ganesan, V. Thangavel, W.S. Yoon, Y.S. Lee, A.C.S. Appl, Energy Mater. 4 (12) (2021) 13376–13394, https://doi.org/10.1021/acsaem.1c02099.
[7] M. Lin, M. Deng, C. Zhou, Y. Shu, L. Yang, L. Ouyang, Q. Gao, M. Zhu, Electrochim. Acta 309 (2019) 25–33, https://doi.org/10.1016/j.electacta.2019.04.070.
[8] M. Fu, Q. Jiao, Y. Zhao, J. Mater. Chem. A 1 (18) (2013) 5577–5586, https://doi.org/10.1039/c3ta10402h.
[9] F. Xie,, L. Zhang,, C. Ye,, M. Jaroniec,, S.Z. Qiao, Adv. Mater. 31(38) (2019) 1–8. 10.1002/adma.201800492.P. Nagajyothi, *Chem. Chem. Phys.*, **18** (2), 2015, 926–931.
[10] P. Poizot, S. Laruelle, S. Grugeon, L. Dupont, J.M. Tarascon, Nature 407 (6803) (2000) 496–499, https://doi.org/10.1038/35035045.
[11] J. Yao, Y. Gong, S. Yang, P. Xiao, Y. Zhang, K. Keyshar, G. Ye, S. Ozden, R. Vajtai, P. M. Ajayan, ACS Appl. Mater. Interfaces 6 (22) (2014) 20414–20422, https://doi.org/10.1021/am505983m.
[12] G.N. Sureshbabu, N.K. Shakkeel, N. Kalaiselvi, J. Alloys Compd. 877 (2021), https://doi.org/10.1016/j.jallcom.2021.160306.
[13] P. Zhang, X. Zhang, G. Li, Ionics (Kiel) 26 (1) (2020) 393–401, https://doi.org/10.1007/s11581-019-03221-z.
[14] S.S. Kim, S. Ogura, H. Ikuta, Y. Uchimoto, M. Wakihara, Solid State Ion. 146 (3–4) (2002) 249–256, https://doi.org/10.1016/S0167-2738(01)01013-X.
[15] K. Bin Masood, G. Parte, N. Jain, P.K. Dwivedi, P. Kumar, M.V. Shelke, R.P. Patel, J. Singh, J. Taiwan Inst. Chem. Eng. 112 (2020) 60–66, https://doi.org/10.1016/j.jtice.2020.07.009.
[16] L. Gao, G. Chen, L. Zhang, B. Yan, X. Yang, Electrochim. Acta 379 (2021), https://doi.org/10.1016/j.electacta.2021.138185 138185.
[17] L. Shen, E. Uchaker, C. Yuan, P. Nie, M. Zhang, X. Zhang, G. Cao, ACS Appl. Mater. Interfaces 4 (6) (2012) 2985–2992, https://doi.org/10.1021/am300357b.
[18] F. Wu, X. Wang, M. Li, H. Xu, Ceram. Int. 42 (15) (2016) 16666–16670, https://doi.org/10.1016/j.ceramint.2016.07.099.
[19] J. Guo, H. Zhu, S. Zhou, Y. Sun, X. Zhang, Ionics (Kiel) 21 (10) (2015) 2993–2999, https://doi.org/10.1007/s11581-015-1532-x.
[20] Y. Zhao, F. Wang, C. Wang, S. Wang, C. Wang, Z. Zhao, L. Duan, Y. Liu, Y. Wu, W. Li, D. Zhao, Nano Energy 56 (November 2018) (2019) 426–433, https://doi.org/10.1016/j.nanoen.2018.11.040.
[21] H. Liu, B. Liu, H. Guo, M. Liang, Y. Zhang, T. Borjigin, X. Yang, L. Wang, X. Sun, Nano Energy 51 (June) (2018) 639–648, https://doi.org/10.1016/j.nanoen.2018.07.021.
[22] X. Liu, Y. Hao, J. Shu, H.M.K. Sari, L. Lin, H. Kou, J. Li, W. Liu, B. Yan, D. Li, J. Zhang, X. Li, Nano Energy 57 (2019) 414–423, https://doi.org/10.1016/j.nanoen.2018.12.024.
[23] R. Thangavel, M. Moorthy, B.K. Ganesan, W. Lee, W.S. Yoon, Y.S. Lee, Small 16 (2020) 41, https://doi.org/10.1002/smll.202003688.
[24] M.S. Park, G.K. Veerasubramani, R. Thangavel, Y.S. Lee, D.W. Kim, ChemElectroChem 6 (3) (2019) 653–660, https://doi.org/10.1002/celc.201801517.
[25] R. Thangavel, R. Ponraj, A.G. Kannan, K. Kaliyappan, D.W. Kim, Z. Chen, Y.S. Lee, Green Chem. 20 (21) (2018) 4920–4931, https://doi.org/10.1039/c8gc01987h.
[26] Y. Lu, J. Liang, S. Deng, Q. He, S. Deng, Y. Hu, D. Wang, Nano Energy 65 (2019), https://doi.org/10.1016/j.nanoen.2019.103993 103993.

[27] R. Thangavel, B. Moorthy, D.K. Kim, Y.S. Lee, Adv. Energy Mater. 7 (2017) 14, https://doi.org/10.1002/aenm.201602654.
[28] R. Thangavel, V. Ahilan, M. Moorthy, W.S. Yoon, S. Shanmugam, Y.S. Lee, J. Power Sources 484 (June 2020) (2021), https://doi.org/10.1016/j.jpowsour.2020.229143 229143.
[29] X. Huang, W. Zhang, C. Zhou, L. Yang, H. Wang, Q. Gao, M. Zhu, J. Colloid Interface Sci. 576 (2020) 176–185, https://doi.org/10.1016/j.jcis.2020.05.017.
[30] R. Shanthappa, D. Narsimulu, A.K. Kakarla, J.S. Yu, Int. J. Energy Res. 45 (13) (2021) 19509–19520, https://doi.org/10.1002/er.7052.
[31] Y. Chen, X. Li, K. Park, W. Lu, C. Wang, W. Xue, F. Yang, J. Zhou, L. Suo, T. Lin, H. Huang, J. Li, J.B. Goodenough, Chem 3 (1) (2017) 152–163, https://doi.org/10.1016/j.chempr.2017.05.021.
[32] C. Zhu, Y. Wang, L. Qiu, W. Yang, Y. Yu, J. Li, Y. Liu, J. Alloys Compd. 944 (2023), https://doi.org/10.1016/j.jallcom.2023.169124 169124.
[33] F. Zhang, Y. Shen, M. Shao, Y. Zhang, B. Zheng, J. Wu, W. Zhang, A. Zhu, F. Huo, S. Li, ACS Appl. Mater. Interfaces 12 (2) (2020) 2346–2353, https://doi.org/10.1021/acsami.9b16659.
[34] S.H. Ha, Y.S. Jeong, Y.J. Lee, ACS Appl. Mater. Interfaces 5 (23) (2013) 12295–12303, https://doi.org/10.1021/am4044147.
[35] D.P. Dutta, A. Mathur, J. Ramkumar, A.K. Tyagi, RSC Adv. 4 (70) (2014) 37027–37035, https://doi.org/10.1039/c4ra07618d.
[36] G. Ali, M. Islam, J.Y. Kim, H.G. Jung, K.Y. Chung, ACS Appl. Mater. Interfaces 11 (4) (2019) 3843–3851, https://doi.org/10.1021/acsami.8b16324.
[37] X. Xu, Q. Liu, T. Wei, Y. Zhao, X. Zhang, J. Mater. Sci. Mater. Electron. 30 (5) (2019) 5109–5119, https://doi.org/10.1007/s10854-019-00809-z.
[38] A.K. Gupta, C. Nisoli, P.E. Lammert, V.H. Crespi, P.C. Eklund, J. Phys. Condens. Matter 22 (2010) 33, https://doi.org/10.1088/0953-8984/22/33/334205.
[39] S.M. Tauquir, M. Karnan, K. Subramani, M. Sathish, Mater. Lett. 323 (February) (2022), https://doi.org/10.1016/j.matlet.2022.132563 132563.
[40] S. Wu, R. Xu, M. Lu, R. Ge, J. Iocozzia, C. Han, B. Jiang, Z. Lin, Adv. Energy Mater. 5 (21) (2015) 1–40, https://doi.org/10.1002/aenm.201500400.
[41] L. Zhang, W. He, M. Ling, K. Shen, Y. Liu, S. Guo, Electrochim. Acta 252 (2017) 322–330, https://doi.org/10.1016/j.electacta.2017.08.115.
[42] L. Wan, J. Shen, Y. Zhang, X. Li, J. Alloys Compd. 708 (2017) 713–721, https://doi.org/10.1016/j.jallcom.2017.03.078.
[43] M. Kim, J.F.S. Fernando, Z. Li, A. Alowasheeir, A. Ashok, R. Xin, D. Martin, A. Kumar Nanjundan, D.V. Golberg, Y. Yamauchi, N. Amiralian, J. Li, Chem. Eng. J. 445 (February) (2022), https://doi.org/10.1016/j.cej.2022.136344 136344.
[44] M. Moorthy, M. Karnan, S. Suresh Balaji, S. Gokulnath, M. Sathish, J. Electroanal. Chem. 924 (September) (2022), https://doi.org/10.1016/j.jelechem.2022.116857 116857.
[45] R. Thangavel, A.G. Kannan, R. Ponraj, X. Sun, D.W. Kim, Y.S. Lee, J. Mater. Chem. A 6 (21) (2018) 9846–9853, https://doi.org/10.1039/c8ta00153g.
[46] R. Thangavel, A.G. Kannan, R. Ponraj, G. Yoon, V. Aravindan, D.W. Kim, K. Kang, W.S. Yoon, Y.S. Lee, Energy Storage Mater. 25 (September 2019) (2020) 702–713, https://doi.org/10.1016/j.ensm.2019.09.016.
[47] S. Wu, W. Chen, L. Yan, J. Mater. Chem. A 2 (8) (2014) 2765–2772, https://doi.org/10.1039/c3ta14387b.
[48] B. Wang, S. Li, X. Wu, J. Liu, W. Tian, Phys. Chem. Chem. Phys. 18 (2) (2015) 908–915, https://doi.org/10.1039/c5cp04820f.
[49] Y. Sun, X. Hu, W. Luo, Y. Huang, J. Mater. Chem. 22 (2) (2012) 425–431, https://doi.org/10.1039/c1jm14701c.
[50] J. Haetge, I. Djerdj, T. Brezesinski, Chem. Commun. 48 (53) (2012) 6726–6728, https://doi.org/10.1039/c2cc31570j.
[51] J. Zhou, J. Li, K. Liu, L. Lan, H. Song, X. Chen, J. Mater. Chem. A 2 (48) (2014) 20706–20713, https://doi.org/10.1039/c4ta05073h.
[52] H. Liu, K. Cao, X. Xu, L. Jiao, Y. Wang, H. Yuan, ACS Appl. Mater. Interfaces 7 (21) (2015) 11239–11245, https://doi.org/10.1021/acsami.5b02724.
[53] W. Lu, L. Hao, Y. Wang, Micromachines 13 (2022) 6, https://doi.org/10.3390/mi13060905.
[54] Y. Liu, L. Jiao, Q. Wu, Y. Zhao, K. Cao, H. Liu, Y. Wang, H. Yuan, Nanoscale 5 (20) (2013) 9562–9567, https://doi.org/10.1039/c3nr02850j.
[55] C.T. Cherian, M.V. Reddy, S.C. Haur, B.V.R. Chowdari, ACS Appl. Mater. Interfaces 5 (3) (2013) 918–923, https://doi.org/10.1021/am302583c.
56 S.P. Ong, V.L. Chevrier, G. Hautier, A. Jain, C. Moore, S. Kim, X. Ma, G. Ceder, Energy Environ. Sci. 4 (9) (2011) 3680–3688, https://doi.org/10.1039/c1ee01782a.
[57] T.E. Society, S. Addition, A. Properties, S. Batteries, (2022) 63–67. https://doi.org/10.5796/electrochemistry.23-00012.
[58] G. Jiang, L. Li, Z. Xie, B. Cao, Ceram. Int. 45 (15) (2019) 18462–18470, https://doi.org/10.1016/j.ceramint.2019.06.064.
[59] L. Li, L. Wang, C. Zhang, J. Alloys Compd. 893 (2022), https://doi.org/10.1016/j.jallcom.2021.162336 162336.
60 M. Moorthy, B. Moorthy, B.K. Ganesan, A. Saha, S. Yu, D.H. Kim, S. Hong, S. Park, K. Kang, R. Thangavel, Y.S. Lee, Adv. Funct. Mater. (2023), https://doi.org/10.1002/adfm.202300135(N.d.).(N.d.).
[61] L. Li, G. Dong, H. Zhao, Y. Xu, X.F. Zhang, X. Cheng, S. Gao, L.H. Huo, J. Colloid Interface Sci. 586 (2021) 11–19, https://doi.org/10.1016/j.jcis.2020.10.063.
[62] S.G. Wang, J. Lin, C.Y. Fan, Y.F. Li, J.P. Zhang, X.L. Wu, H.Z. Sun, M.X. Deng, Z.M. Su, J. Alloys Compd. 830 (2020), https://doi.org/10.1016/j.jallcom.2020.154648 154648.